Relative Adipose Tissue Failure in Alström Syndrome Drives Obesity-Induced Insulin Resistance

Tarekegn Geberhiwot,[1,2] Shanat Baig,[1,3] Cathy Obringer,[4] Dorothée Girard,[5] Charlotte Dawson,[1] Konstantinos Manolopoulos,[2] Nadia Messaddeq,[6] Pierre Bel Lassen,[7] Karine Clement,[7] Jeremy W. Tomlinson,[8] Richard P. Steeds,[3] Hélène Dollfus,[4,9] Nikolai Petrovsky,[5,10] and Vincent Marion[11]

METABOLISM

Obesity is a major risk factor for insulin resistance (IR) and its attendant complications. The pathogenic mechanisms linking them remain poorly understood, partly due to a lack of intermediary monogenic human phenotypes. Here, we report on a monogenic form of IR-prone obesity, Alström syndrome (ALMS). Twenty-three subjects with monogenic or polygenic obesity underwent hyperinsulinemic-euglycemic clamping with concomitant adipose tissue (AT) microdialysis and an in-depth analysis of subcutaneous AT histology. We have shown a relative AT failure in a monogenic obese cohort, a finding supported by observations in a novel conditional mouse model (_Alms_$^{flin/flin}$) and ALMS1-silenced human primary adipocytes, whereas selective reactivation of ALMS1 gene in AT of an ALMS conditional knockdown mouse model (_Alms_$^{flin/flin}$; _Adipo-Cre_$^{+/-}$) restores systemic insulin sensitivity and glucose tolerance. Hence, we show for the first time the relative AT failure in human obese cohorts to be a major determinant of accelerated IR without evidence of lipodystrophy. These new insights into adipocyte-driven IR may assist development of AT-targeted therapeutic strategies for diabetes.

Alström syndrome (ALMS) is an ultra-rare (<1 per million) autosomal recessive (OMIM identifier 203800) monogenic metabolic syndrome characterized by childhood-onset obesity, extreme insulin resistance (IR), early-onset type 2 diabetes, accelerated nonalcoholic fatty liver disease, cardiomyopathy, chronic kidney disease, dyslipidemia, and hypertension (1–4). Other hallmarks of ALMS include retinal rod-cone dystrophy and hearing loss (1). ALMS is caused by mutations in ALMS1, a gene encoding the ubiquitously expressed 461-kDa ALMS1 protein (5). We and others have shown that IR in ALMS resembles an extreme form of the metabolic syndrome seen in other obese individuals but is disproportionate to the degree of adiposity and body fat distribution (4,6). Significantly, patients with ALMS are exquisitely sensitive to caloric intake (7) and their metabolic profile of severe IR is similar to that seen in lipodystrophy (8), a condition of partial or complete loss of adipose tissue (AT). The severe metabolic consequences of AT deficiency have been conceptually linked to obesity-related IR by the notion of "adipose expandability" (9). According to this hypothesis, the ability of AT to store excess energy is finite and when this

---

[1]Department of Diabetes, Endocrinology and Metabolism, Queen Elizabeth Hospital Birmingham, Birmingham, U.K.

[2]Institute of Metabolism and Systems Research, University of Birmingham, Birmingham, U.K.

[3]Institute of Cardiovascular Sciences, University of Birmingham, Birmingham, U.K.

[4]INSERM, UMR_U1112, Laboratoire de Génétique Médicale, Université de Strasbourg, Hôpitaux Universitaires de Strasbourg, Fédération de Médecine Translationnelle de Strasbourg, Strasbourg, France

[5]Flinders Medical Centre, Flinders University, Bedford Park, Australia

[6]Institute of Genetics and Molecular and Cellular Biology, CNRS/INSERM, Collège de France, Illkirch, France

[7]NutriOmics Unit, INSERM, Sorbonne Université, Assistance-Publique Hôpitaux de Paris, and Nutrition Department, Pitié-Salpêtrière Hospital, Paris, France

[8]Oxford Centre for Diabetes, Endocrinology and Metabolism, NIHR Oxford Biomedical Research Centre, University of Oxford, Oxford, U.K.

[9]Service de Génétique Médicale et CARGO, Institut de Génétique Médicale d'Alsace, Hôpitaux Universitaires de Strasbourg, Strasbourg, France

[10]Vaxine Pty Ltd, Bedford Park, Australia

[11]INSERM, UMR_U1112, Ciliopathies Modeling and Associated Therapies Group, Laboratoire de Génétique Médicale, Fédération de Medecine Translationelle de Strasbourg, Strasbourg, France

Corresponding authors: Tarekegn Geberhiwot, tarekegn.hiwot@uhb.nhs.uk, and Vincent Marion, vincent.marion@inserm.fr

limit is reached, whether at very low absolute levels in lipodystrophy or at high absolute levels as in obesity, lipotoxicity of AT and other organs ensues (9–11). Despite the conceptual appeal of the notion that obesity-related metabolic disease arises from relative AT capacity failure, no human examples of obesity with disproportionate metabolic complications due to constraint of AT expansion have been described. Currently, it is not known how the underlying molecular defects in ALMS result in severe IR or whether AT dysfunction plays a role in IR. In an ALMS mouse model, a GLUT4 glucose transport defect was proposed as an early sign of metabolic alterations (12), although others using ALMS1-silenced human preadipocytes reported that proximal signaling events in response to insulin were unaffected in the absence of ALMS1 (13).

We hypothesized that AT dysfunction may be a key determinant of accelerated IR in our monogenic obese human ALMS cohort. To test this hypothesis, we used an integrative physiological approach to assess intermediary metabolism and subcutaneous AT (sAT) structure and function in ALMS and matched polygenic obese control subjects. To gain further insight into the role of ALMS1 in adipocyte dysfunction, we generated an ALMS mutant mouse model and then selectively reactivated ALMS1 gene just in the adipocyte tissue. Selective reactivation of ALMS1 in AT restored the whole systemic IR.

RESEARCH DESIGN AND METHODS

Clinical, Biochemical, and Imaging Assessment
The human study took place in the National Institute for Health Research/Wellcome Trust Clinical Research Facility, Birmingham, U.K. Weight was measured using the same digital weighing scale at all study visits, height was measured using a stadiometer, and BMI was calculated as weight in kilograms divided by the square of height in meters. Waist circumference (WC) was measured with the subject in an erect posture just above the iliac crest. Blood was collected after a 12-h fast, and plasma and serum were separated immediately and stored at $-80°C$. Hemoglobin A_{1c} (HbA$_{1c}$), insulin, C-peptide, free fatty acids (FFA), enhanced liver fibrosis (ELF) test, and adipokines (adiponectin and leptin) were analyzed as previously described. Liver stiffness was assessed by transient elastography (FibroScan; Echosens, Paris, France) as previously described (34).

Hyperinsulinemic-Euglycemic Clamp
Hyperinsulinemic-euglycemic clamping (HEC) was commenced at 0900 h after an overnight fast. Glucose concentrations were measured in arterialized blood. Participants were given a bolus (2 mg/kg) of D-glucose (U-^{13}C) (Cambridge Isotope Laboratories, Cambridge, U.K.) followed by continuous infusion (0.02 mg/kg/min) for 4 h. During the first 2 h (basal phase), blood glucose was checked every 15 min and steady-state blood samples were taken after 90, 105, 120 min for measurement of insulin, FFA, and stable isotopes. At 120 min, an insulin infusion (Actrapid; Novo Nordisk, Copenhagen, Denmark) was commenced at

a rate of 40 mU/m^2/min for 2 h. At 124 min, 20% dextrose solution with [^{13}C]-glucose (enriched to 4%) was infused. The rates of hepatic glucose production and glucose disposal were calculated with a modified version of the Steele equations (35).

Serum [U-^{13}C]-glucose enrichment was determined by gas chromatography–mass spectrometry (gas chromatography, Agilent 6890N, and mass spectrometry, Agilent 5973N; Agilent Technologies). Glucose was extracted with use of methanol-chloroform and hydrochloric acid, dried under nitrogen gas, and then derivatized using the heptofluorobuyric acid method as previously described (37). The glucose derivative was acquired by selection of ion monitoring at mass-to-charge ratios (m/z) 519 and 525 for unlabeled and [U-^{13}C]-glucose, respectively. Serum [U-^{13}C]-glucose enrichment was determined using a standard curve for [U-^{13}C]-glucose.

AT Microdialysis
A microdialysis catheter (CMA 63; M Dialysis AB, Stockholm, Sweden) was inserted 10 cm lateral to the umbilicus and connected to a microdialysis pump containing an isotonic fluid, Perfusion Fluid T1 (M Dialysis AB), which was infused at a fixed rate of 0.3 μL/min. A microvial was connected to the exit end, and samples were collected every 30 min throughout the clamp procedure. Glycerol, lactate, and pyruvate concentrations were measured in microdialysate with an enzyme-kinetic analyzer (CMA Iscus Flex). The rate of interstitial glycerol appearance was taken to reflect the rate of sAT lipolysis (36).

AT Biopsy and Analysis
sAT biopsies were collected from the periumbilical region. Samples were preserved in 4% formalin solution and subsequently embedded in paraffin. Fixed samples were sectioned in 5-μm slices and stained with hematoxylin-eosin for determination of adipocyte morphology. Picrosirius red staining was used to assess fibrosis and CD68 and CD163 immunostaining to assess macrophage infiltration.

Analysis of fibrosis was undertaken by histomorphometry with use of Calopix (TRIBVN Healthcare, Châtillon, France) with content color thresholds. Total fibrosis was expressed as a ratio of total AT area, as described by Divoux et al. (37). Pericellular fibrosis was assessed in 10 fields of 250 × 250 μm and expressed as a ratio of the sum of field surfaces. Histological scoring of fibrosis was also applied as described by Bel Lassen et al. (38,39). Adipocyte images were obtained at ×40 magnification, and morphological analyses were performed with use of Adiposoft software (Center for Applied Medical Research, University of Navarra). Adipocyte size and number were measured in two fields of 1,000 × 1,000 μm using a validated, optimized sequence of image analysis steps in Adiposoft. On average 267 adipocytes were measured per participant.

Reagents and Kits
2-(N-7-nitrobenz-2-oxa-1,3-diazol-4-yl)amino)-2-deoxy-glucose (2-NBDG) was from Molecular Probes, Invitrogen,

and Hoechst 33258, cat. no. H3569 and C10587, was from LifeTech. AdipoRed Assay Reagent was from Lonza (cat. no. PT-7009; Lonza, Basel, Switzerland). Lentiviral particles were from Santa Cruz Biotechnology: ALMS1 shRNA (h) Lentiviral Particles (cat. no. sc-72345-V) and Control shRNA Lentiviral Particles-A (cat. no. sc-108080). A glucose uptake assay kit (Colorimetric) was from Abcam (cat. no. ab136955). The ELISA Kit for Leptin (LEP) was from Cloud-Clone (cat. no. SEA084Mu).

In Vivo Mouse Studies

Animal studies were performed in accordance with the recommendations in the Australian Code of Practice for the Care and Use of Animals for Scientific Purposes of the National Health and Medical Research Council. $Alms1^{foz/foz}$ (fat aussie [FA]) mice and $Alms1^{+/+}$ [wild type]) littermates were maintained on a C57BL/6J background in the animal facility at Flinders Medical Centre under pathogen-free conditions in a 12-h light/dark cycle. Mice had free access ad libitum to water and either normal chow (rat and mouse maintenance pellets, Gordon's Specialty Stock Feeds, Yanderra, Australia). Primers flanking the foz mutation were used for PCR genotyping: forward, ACA ACT TTT CAT GGC TCC AGT; reverse, TTG GCT CAG AGA CAG TTG AAA. The $Alms^{flin/flin}$ mouse model was generated using the EUCOMM/KOMP-CSD ES cell with the promoter driven line, with further details available from https://www.knockoutmouse.org/about/eucomm. Briefly, the corresponding MGI allele was the $Alms1^{tm1a(EUCOMM)tm1e}$. The ES cell strain on a C57BL/6N background with IKMC project number 27978 was used for blastocyst injection. The targeting vector used was the PRPGS00084_A_C01. Following mouse production, the resulting modified allele, corresponding to the $Alms^{flin/flin}$ modified allele, contained the Frt-lacZ-LoxP-Neo-Frt-LoxP sequence between exon 6 and exon 7 of the $Alms1$ gene without the third loxP after exon 7. The C57BL/6J congenic strain for the adiponectin-Cre expressing mouse line was obtained from The Jackson Laboratory, under the reference number 010803-B6; FVB(Adipoq-cre)1Evdr/J, stock no. 010803. All animals were housed in a temperature- and humidity-controlled facility, with a 12-h light/12- h dark cycle and feeding with chow diet (LM-485; Harlan Teklad Premier Laboratory Diets) and tap water ad libitum. Mice were tested for IR by insulin tolerance test (ITT) and intraperitoneal glucose tolerance test (GTT). The ITT was performed in 4-h-fasted mice. Insulin (Humulin R; Eli Lilly) was injected intraperitoneally at 0.5 units/kg body wt in 0.9% saline (Pfizer). The GTT was performed in 18-h-fasted mice. Glucose was injected, 2 g/kg body wt, in 0.9% saline. The tail was snipped for blood collection, and the plasma glucose was determined at 0, 15, 30, 60, and 120 min in the GTT with a glucometer (Optium Xceed; Abbott). Alternatively, plasma insulin measurement was performed with blood from 4-h-fasted mice collected from conscious animals via submandibular bleeding and analyzed for fasting insulin with a commercial ultrasensitive mouse insulin ELISA kit (Crystal Chem). Mice were sacrificed by cervical dislocation.

Insulin-Dependent Glucose Uptake

High-fat-fed (Specialty Feed, cat. no. SF03-020; 23% fat, 0.19% cholesterol, simple carbohydrates, based on AIN93G) mice were fasted for 3–6 h before start of experiment. Insulin (0.75 units/kg) was injected intravenously via the tail vein in combination with 3 μCi of 2-[1-C (14)] deoxy-D-glucose (PerkinElmer, Melbourne, Australia). Blood glucose and samples were collected at 0, 5, 10, 15, 20, 40, and 60 min after injection from the tail. Mice were sacrificed (cervical dislocation), and liver, muscle (both sides soleus, and extensor digitorum longus = glycolytic muscles; left thigh), heart, SAT, and visceral AT (peri-renal) were isolated and rinsed in ice-cold PBS, quickly dried on flint-free paper tissue, and weighed. Then, a piece of the isolated tissue was chopped into small pieces, weighed again, homogenized for 1 h at 60°C in 1 N NaOH, and then neutralized with HCl (1 mol/L). One part of the homogenate was used for determination of deoxyglucose + deoxyglucose-6-phosphate by precipitating proteins with 6% perchloro acid and the supernatant measured by scintillation counter (PerkinElmer). The other part was mixed with 0.3 N $ZnSO_4$ to react with deoxy-glucose-6-P, and the complex was precipitated with 0.3 N $Ba(OH)_2$ and the supernatant used for scintillation measurement.

AdipoRed Staining of AT

Fat tissue of 60-day-old and 120-day-old mice was isolated and briefly washed in PBS (3.2 mmol/L Na_2HPO_4, 0.5 mmol/L KH_2PO_4, 1.3 mmol/L KCl, and 135 mmol/L NaCl, pH 7.4). Samples were then placed in 4% paraformaldehyde (in 0.1 mol/L sodium phosphate buffer, pH 7.2) for 15 min, washed in PBS and incubated in AdipoRed dye (1/25; Lonza) with 30 μmol/L DAPI (Sigma-Aldrich) for 15 min. After three washes with PBS, samples were mounted on slides and pictures were taken using Zeiss Axio Imager fluorescence microscope.

FFA Measurement

Plasma (10 μL) was spiked with 5 μL fatty acid standard mix containing 260 ng myristic acid-d3, 1,128 ng palmitic acid-d3, 840 ng stearic acid-d3, 650 ng linoleic acid-d4, 1.04 ng arachidic acid-d3, 432 ng arachidonic acid-d8, 650 ng behenic acid-d3, 108 ng DHA-d5, 0.52 ng lignoceric-d4, and 0.4 ng cerotic acid-d4. Plasma was mixed with 1.2 mL Dole extraction solvent (2 mol/L of 40/10/1 v/v/v isopropanol/hexane/phosphoric acid) and vigorously mixed for 5 min. FFAs were finally extracted with 1 mL hexane and 1.5 mL distilled water. Analysis was conducted by gas chromatography–mass spectrometry operating in negative chemical ionization mode as previously described.

Cell Culture

Human white visceral preadipocytes (cat. no. C-12732; PromoCell) were purchased. The preadipocytes were

seeded according to the manufacturer's protocol and cultured in the preadipocyte growth medium (cat. no. C-27410; PromoCell) to confluence. One day before induction of terminal adipogenesis, the cells were infected with specific lentiviral particles, and on the next day adipogenic differentiation was induced with preadipocyte differentiation medium (cat. no. C-27436; PromoCell) for 2 days. After the differentiation phase, the medium was finally changed to the Adipocyte Nutrition Medium.

RNA Extraction, cDNA Synthesis, Quantitative PCR, and TaqMan

Total RNA was prepared from the different tissues and cells with a RiboPure kit (cat. no. AM1924; Ambion) followed by a DNAse treatment with TURBO DNA-free (cat. no. AM 1907; Ambion). RNA integrity was assessed by gel electrophoresis and RNA concentration by Eppendorf BioPhotometer plus with the Hellma Tray Cell (cat. no. 105.810-uvs; Hellma). Reverse transcription of 1 μg total RNA to cDNA was performed using the Bio-Rad iScript cDNA Synthesis Kit (cat. no. 170-8891; Bio-Rad Laboratories). Real-time quantitative PCR amplification was performed in a Bio-Rad CFX96 Real-Time System using the iQ SYBR Green Supermix (cat. no. 170-8886; Bio-Rad Laboratories) and primer sets optimized for tested targets for SYBR Green–based real-time PCR for the real-time PCR. TaqMan analysis was carried out with the specific gene assay with the TaqMan Fast Advanced Master Mix (cat. no. 4444557; Applied Biosystems).

Western Blots and Immunofluorescence Microscopy

Tissues were harvested after anesthesia-overdosing euthanasia, and proteins were extracted with use of the radioimmunoprecipitation assay buffer (50 mmol/L Tris, 150 mmol/L NaCl, 0.1% SDS, 1% Triton-X100; pH 7.4) supplemented with cOmplete Mini Protease Inhibitor Cocktail and PhosSTOP phosphatase inhibitor cocktail (Roche, Rotkreuz, Switzerland). Samples were homogenized, sonicated, and centrifuged 30 min at 17,000g, 4°C, for 30 min. Protein concentration was determined by BCA Assay (Thermo Fisher Scientific). Samples were boiled at 99°C for 10 min, and 25 μg protein was loaded per lane. Cellular proteins from cells were obtained by trichloroacetic acid precipitation, and immunoblot analyses were performed with use of 30–50 μg total protein. Specific antibody binding was visualized with use of the SuperSignal West Femto Maximum Sensitivity Substrate (cat. no. Lf145954; Pierce) on a Bio-Rad VersaDoc Imaging System. Ponceau S staining of gel lanes was used as loading control and to normalize the signal obtained after specific immunodetection of the protein of interest using the Bio-Rad Quantity One program. For immunofluorescence experiments, the cells were seeded on Permanox eight-well Lab-Tek II Chamber Slide (cat. no. 177445, Nunc). Cells were treated as indicated, and then both cells and tissues cryosections were processed for protein detection after methanol fixation and permeabilized with 0.1% Triton X-100. The microscopy slides were mounted for detection with VECTASHIELD Mounting Medium (cat. no. H-1200; Vector Laboratories). For viewing of immune-detected proteins, cells were formalin fixated for 15 min and were directly blocked, followed by immunostaining and acquisition with an upright Zeiss Axio Imager Z2 microscope.

Statistical Analysis

The required sample size (number of animals per group) to detect a statistically significant effect with a two-tailed Student t test was calculated based on the sample size determination method. Type I error probability was at 0.05 and with a power of 0.90. Depending on which technique was used, the minimum difference considered meaningful was set between 10 and 15% with an anticipated coefficient of variation between 5 and 10. In most experiments, the investigators were not blinded to sample identity. Data are presented as mean ± SE when normally distributed or median with interquartile range (IQR) otherwise. Categorical variables are reported as numbers and percentages. Unpaired Student t test (or, where appropriate, its nonparametric equivalent) was used to compare independent groups. Area under the curve (AUC) analysis was performed with use of the trapezoidal method for interstitial glycerol, lactate, and pyruvate release during the clamp. The Shapiro-Wilk test was used to determine the normality of the distribution in all cases where a parametric test was used. In the event that the normality assumption failed, the Wilcoxon signed rank test was used instead. The significance level for this study was set at $P < 0.05$. Statistical analyses were performed using GraphPad Prism 5 software (GraphPad Software, Inc.) and SPSS statistical software, version 24.

Data and Resource Availability

The data sets generated during and/or analyzed during the current study are available from the corresponding author upon reasonable request.

RESULTS

Baseline Characteristics of Study Participants

All participants with ALMS had disease-causing pathogenic mutations and met clinical diagnostic criteria (Supplementary Table 1). Anthropometric, clinical, and metabolic characteristics are shown in Table 1. There was no difference between ALMS participants and obese control subjects in terms of age, sex, weight, BMI, and WC. In line with participants with severe IR, most ALMS participants had type 2 diabetes and advanced nonalcoholic fatty liver disease compared with none of the control subjects. ALMS participants were also more likely to have hypertension and an atherogenic lipid profile (Table 1). Surrogate markers of IR (fasting glucose and insulin and HOMA of IR [HOMA-IR]) were all high and QUICKI was low in

Table 1—Demographic and clinical characteristics of study participants and control subjects with common obesity

Patient characteristics	Subjects with ALMS ($n = 12$)	Control subjects ($n = 11$)	P
Age (years)	26.5 ± 9.7	29.7 ± 4.2	0.33
Male, n (%)	67	72	0.14
Weight (kg)	76.3 ± 14.4	88.1 ± 16.9	0.09
BMI (kg/m^2)	30.3 ± 6.2	29.9 ± 4.2	0.86
WC (cm)	96 ± 12	100 ± 13	0.41
Subjects with diabetes, %	67	0	—
Systolic BP (mmHg)	121 ± 11	120 ± 12	0.77
Glucose (mmol/L)	8.6 ± 5	4.8 ± 0.5	0.02
Insulin (pmol/L)	360 (245–478)	31 (18–62)	<0.001
HOMA-IR	14.2 ± 9.6	1.2 ± 0.7	<0.001
QUICKI	0.28 ± 0.05	0.38 ± 0.04	<0.001
M (mg/kg/min)	1.94 ± 0.87	4.86 ± 2.37	<0.001
Gd (mg/kg/min)	1.25 ± 0.85	3.65 ± 1.81	<0.001
EGP (mg/kg/min)	1.6 (1.4–2.4)	0.3 (0–1.9)	0.03
Hepatic insulin sensitivity disposition index	0.002 ± 0.002	0.01 ± 0.01	<0.001
NEFA (mmol/L)	0.72 ± 0.25	0.58 ± 0.23	0.18
NEFA postinsulin (mmol/L)	0.14 ± 0.09	0.02 ± 0.02	<0.001
NEFA_half_max	511 ± 355	55 ± 24	0.00
Adipose ISI (mmol/L $\times$ pmol/L)	244.3 ± 169.4	23.27 ± 17.22	0.00
Adiponectin (ng/mL)	$1,478 \pm 756$	$7,310 \pm 3,823$	<0.001
Leptin (ng/mL)	15.3 ± 11	5.8 ± 4.7	0.0259
Ratio of adiponectin (μg/mL) to leptin (ng/mL)	136 ± 108	$2,960 \pm 3,052$	0.006
Cholesterol (mmol/L)	4.4 ± 1	4.4 ± 0.9	0.94
Triglyceride (mmol/L)	2.8 ± 2	1.3 ± 0.6	0.03
HDL cholesterol (mmol/L)	0.7 ± 0.2	1.2 ± 0.2	<0.001
Alanine transferase units/L	86.8 ± 55.2	19.3 ± 8.7	<0.001
Aspartate transferase units/L	41.5 ± 23	18.5 ± 3.7	0.01
ELF score	9.1 ± 1.3	7.4 ± 0.7	<0.001
Transient elastography (kpa)	9.35 (6.8–12.93)	4.9 (3.3–7.1)	0.05
IHD, n (%)	2 (17)	0 (0)	—
Insulin, n (%)	2 (17)	0 (0)	—
Oral hypoglycemic, n (%)	10 (83)	0 (0)	—
Antihypertensive agents, n (%)	11 (92)	0 (0)	—
Lipid-lowering agents, n (%)	5 (42)	0 (0)	—

Data are means $\pm$ SE or median (IQR) unless otherwise indicated. BP, blood pressure; EGP, endogenous (hepatic) glucose production; Gd, glucose disposal; IHD, ischemic heart disease; ISI, insulin sensitivity index; NEFA, nonesterified fatty acid.

ALMS participants ($P < 0.001$ for all) (Table 1). ALMS participants had significantly lower plasma adiponectin (mean $\pm$ SE $1,479 \pm 756$ vs. $7,311 \pm 3,824$ [$P < 0.001$]) and higher leptin concentrations (15 ± 11 vs. 5.8 ± 4.8 [$P = 0.026$]).

Participants With ALMS Have Severe Muscle and Hepatic IR

HEC (Fig. 1A and B) revealed that ALMS participants required lower weight-adjusted glucose infusion rates in response to insulin (mean $\pm$ SE 1.9 ± 0.8 vs. control subjects 4.8 ± 2.3 mg/kg/min; $P < 0.001$) and had lower weight-adjusted glucose disposal rates (1.2 ± 0.8 vs. control subjects 3.6 ± 1.8 mg/kg/min; $P < 0.01$), indicating severe muscle IR in ALMS participants versus obese controls. Endogenous (hepatic) glucose production rates were higher in ALMS participants than obese control subjects (1.65 mg/kg/min [IQR 1.4–2.9] vs. 0.3 mg/kg/min (0.03–1.9); $P = 0.02$) (Fig. 1C). Furthermore, the hepatic insulin sensitivity disposition index for ALMS participants

was lower (0.002 ± 0.002 vs. 0.024 ± 0.01 mg/kg/min/mL; $P < 0.001$) (Fig. 1*D*).

AT From ALMS Participants Has Altered Structure and Is Severely Dysfunctional

sAT releases the majority of circulating nonesterified fatty acids (NEFA). Systemic NEFA concentrations were similar in ALMS and control subjects in the fasting state but were significantly higher in ALMS than in obese control subjects after insulin infusion (mean $\pm$ SE 0.14 ± 0.09 vs. 0.03 ± 0.04 mmol/L ($P = 0.001$) (Fig. 1*E* and *F*). This difference between the two cohorts became more pronounced when we took into account the level of fasting insulin by deriving the AT IR index (ADIPO-IR) (ADIPO-IR = fasting NEFA × fasting insulin) (14). ADIPO-IR in ALMS participants was nearly 10-fold higher than in obese control subjects (244.3 ± 169.4 vs. 23.2 ± 17.2 mm/pmol/L; $P < 0.0001$)) (Fig. 1*G*). For quantification of AT insulin sensitivity, regression analysis was used to establish the insulin concentration causing half-maximal suppression of serum NEFA; this concentration was eightfold higher in ALMS participants than in obese control subjects (506 pmol/L [IQR 239.2–717.7] vs. 62 [27–70]; $P < 0.0001$), confirming the extreme AT IR in ALMS (Fig. 1*H*). The responsiveness of sAT lipolysis to insulin was quantified by direct measurement of interstitial glycerol concentration using microdialysis during the HEC (Fig. 2*A*). In the fasting state, the rate of increase in interstitial glycerol concentration was not different in ALMS participants and obese control subjects ($P = 0.05$). In control subjects, insulin infusion suppressed the rate of interstitial glycerol release (basal AUC 240 ± 88 μmol/L · h vs. postinsulin AUC 163 ± 80 μmol/L · h; $P < 0.001$), but insulin failed to suppress glycerol release in ALMS participants (basal AUC 309 ± 84 μmol/L · h vs. postinsulin AUC 279 ± 95 μmol/L · h; $P = 0.26$). Furthermore, the sAT interstitial fluid lactate-to-pyruvate ratio (an established marker of mitochondrial dysfunction and oxidative stress) (15,16) was markedly elevated in ALMS participants (Fig. 2*B*). Taken together, these observations provide compelling evidence for dynamic AT dysfunction in ALMS. sAT histology studies showed that adipocyte size was on average larger in ALMS participants than obese control subjects ($6,033 + 875$ vs. $4,346 \pm 880$ μm^2; $P < 0.001$) (Fig. 2*C* and *D*). Multiorgan fibrosis is a recognized feature of ALMS end-stage disease, and in murine models, primary alterations in extracellular matrix can influence adipose expandability (17). sAT from ALMS participants, however, showed no excess fibrosis whether quantified as pericellular or total fat scores (Supplementary Fig. 1).

AT IR Specifically Drives the Type 2 Diabetes Phenotype in ALMS Mouse Model

The FA is a mutant mouse model of ALMS caused by a spontaneous 10-bp deletion and premature stop codon in exon 8 of ALMS1. Similar to human ALMS patients, FA mice develop obesity, hyperinsulinemia, and diabetes in early adolescence (18). We first used FA mice to identify the temporal relationship between onset of obesity, hyperinsulinemia, and impaired glucose tolerance, as well as to examine for insulin-signaling defects in insulin-responsive tissues that could be secondary to the ALMS1 mutation. In comparison with age-matched wild-type littermates, 6-month-old FA mice were obese (mean $\pm$ SE 45.5 ± 1.7 vs. 26.4 ± 1.3 g; $P < 0.05$) (Fig. 3*A*), although contrary to the adipocyte hyperplasia that underlies common obesity, obesity in the FA was reflected in adipocyte hypertrophy, similar to human ALMS data observations (Fig. 3*B*). Like humans, obese FA mice exhibited fasting hyperglycemia and were highly insulin resistant on ITT compared with their littermates (ITT) (Fig. 3*C*). Two-month-old FA mice prior to development of obesity and adipocyte hypertrophy (Fig. 3*D* and *E*) already exhibited fasting hyperglycemia and IR on ITT (Fig. 3*F*), consistent with IR preceding rather than following obesity. Immunodetection of IRAP, AKT, phosphorylated AKT, GLUT4, and C/EBP-α in insulin-responsive tissues (heart, liver, skeletal muscles, and white AT [WAT]) from 6-month-old nonfasted FA mice showed an increased phosphorylated AKT–to–AKT ratio in WAT only (Fig. 3*G*), consistent with an increase rather than reduction in insulin receptor activation and signaling in the proximal end of the insulin pathway. Insulin-stimulated deoxyglucose uptake studies confirmed impaired uptake restricted to WAT in FA with compensatory increased deoxyglucose uptake by muscle (Fig. 3*H*), pointing to a specific defect in adipocyte glucose transport as the primary site of IR in FA mice. Consistent with the human data, the 6-month-old FA mice showed elevated circulating levels of leptin (Supplementary Fig. 2*A*). Further metabolic characterization of the FA mice showed that the circulating lipid profile was also altered with significant decrease in the FFAs C16:0, C18:2 n-6, C18:1 n-9, and C18:1 n-7 in the FA mice plasma compared with controls (Supplementary Fig. 2*B*), a metabolic effect associated with increased lipid droplets denoting liver steatosis in the Alms mutant mice (Supplementary Fig. 2*C*).

Adipocyte-Specific Reactivation of ALMS1 Reverses Type 2 Diabetes Phenotype in a Mouse Model of ALMS

To explore the exact contribution of AT in the metabolic phenotype of ALMS, we generated an *ALMS* mouse model where a targeting cassette containing encoding elements for β-galactosidase (lacZ gene), the neomycin-resistance gene (neo), FRT, and loxP sites was inserted between exons 6 and 7 of the *Alms1* gene (Supplementary Fig. 3*A*, top). This specific insertion resulted in an Alms1 knockout model termed *Alms*$^{flin/flin}$ with no tissue *Alms1* mRNA detectable by real-time PCR (Fig. 4*A*). Subsequently, we bred the *Alms*$^{flin/flin}$ mice with the Adiponectin-Cre mouse, whose specific Cre activity was validated by a separate breeding with the RosaTomato-eGFP mouse line depicting Cre recombinase activity only in the adipocytes (Supplementary Fig. 3*B*), to remove the floxed neo gene (Supplementary Fig. 3*A* and bottom Supplementary Fig. 3*C*). The
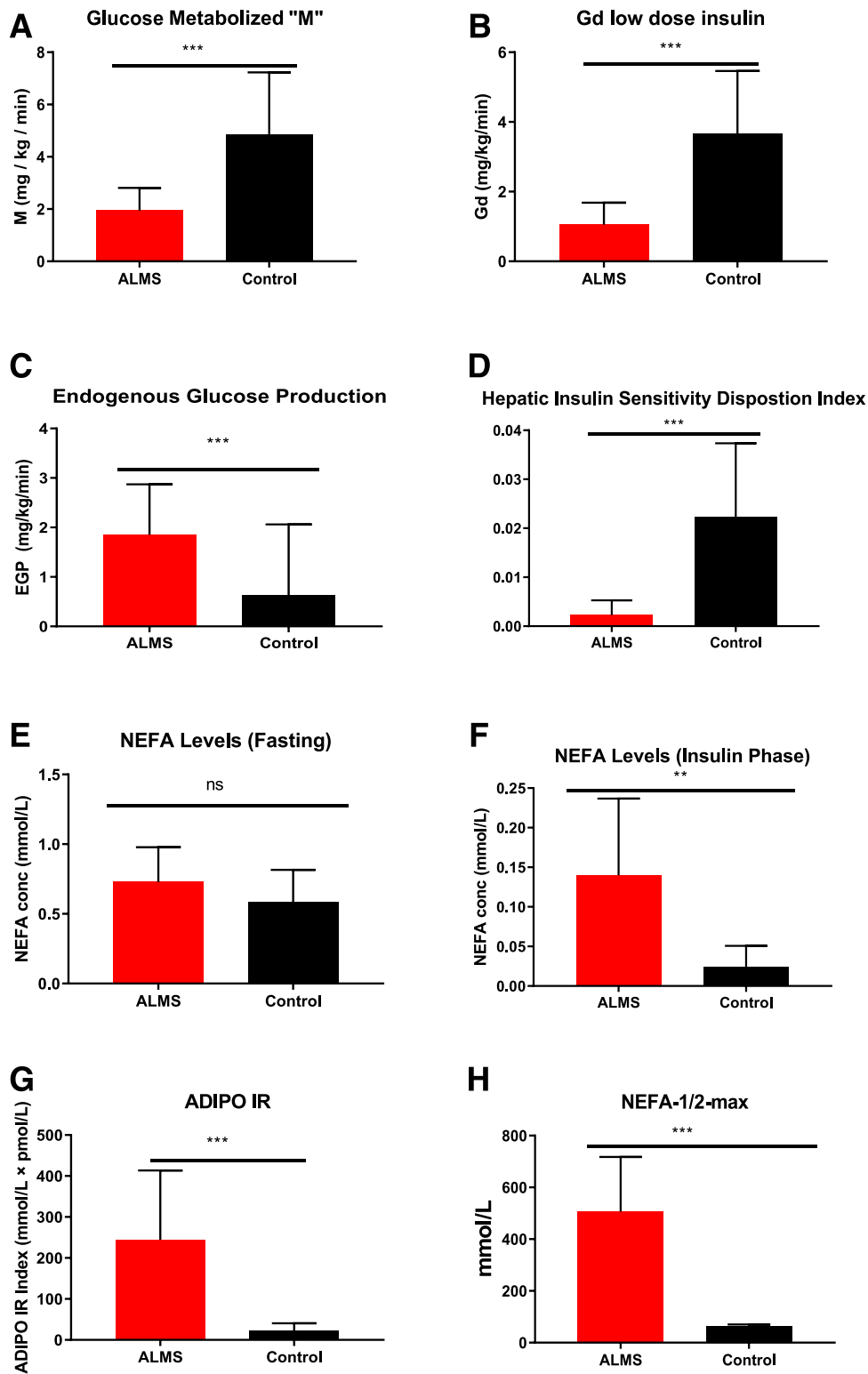
Figure 1—Metabolic parameters of human subjects included in this study. *A–D*: HEC markers of IR. *E–H*: NEFA concentration (conc) and Adipo-IR (fasting NEFA [mmol/L] × fasting insulin [pmol/L]) as measured during insulin clamp. Data are presented as *n* (%), median (IQR), or mean ± SD, as applicable. Significance was set at $P < 0.05$. **$P < 0.01$, ***$P < 0.001$.
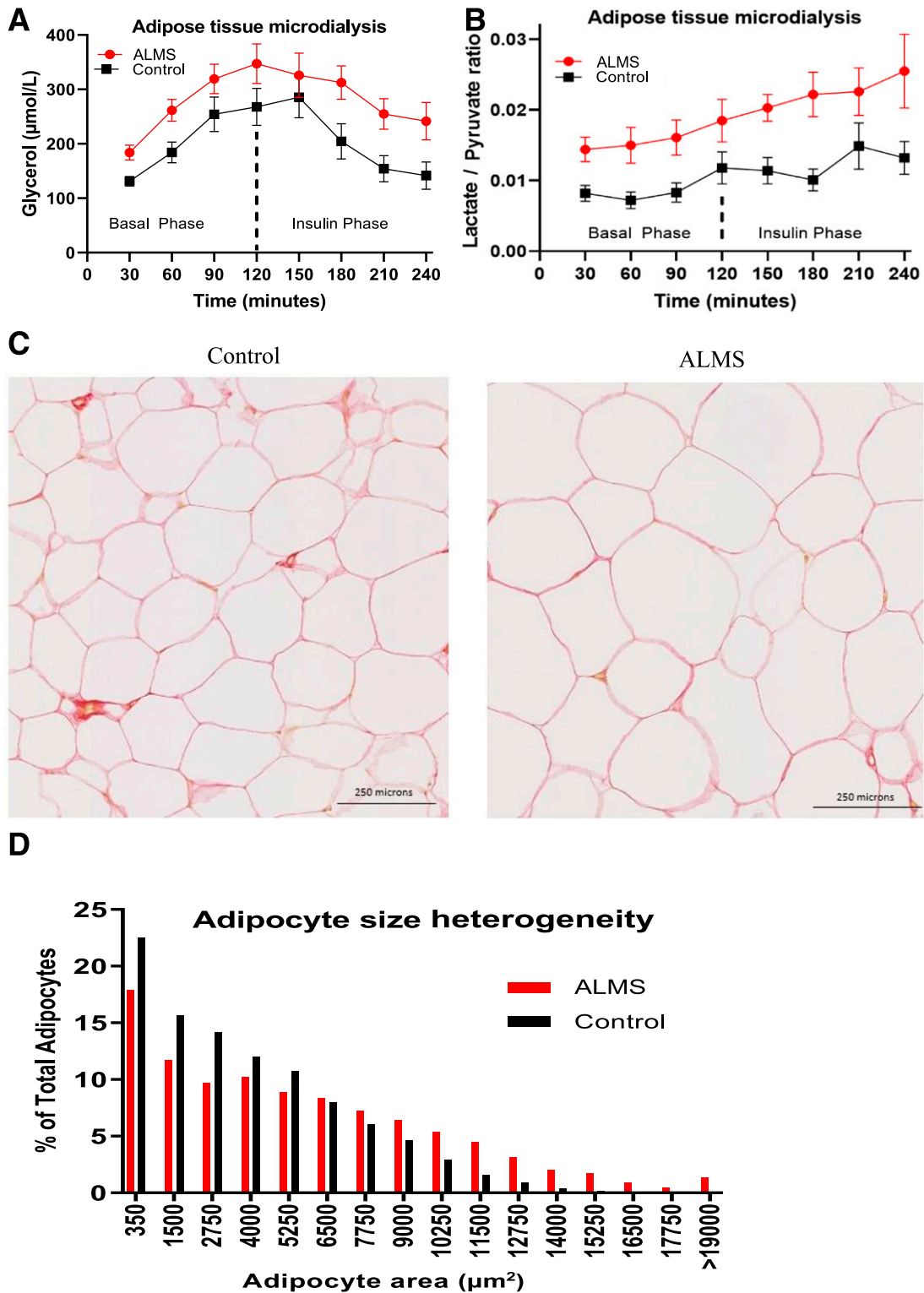
Figure 2—AT characteristic of patients with ALMS and matched control subjects. *A*: Changes in glycerol levels measured in sAT interstitial fluid during insulin clamp at the basal and insulin phase. Values shown are mean and SEM (AUC basal phase 0.01, AUC insulin phase $P <$ 0.001). *B*: Lactate-to-pyruvate ratio AUC basal phase 0.01, AUC insulin phase 0.03). *C* and *D*: sAT histology revealed significant heterogeneity observed in adipocyte size in ALMS compared with obese control subjects as seen on hematoxylin-eosin staining of sAT.
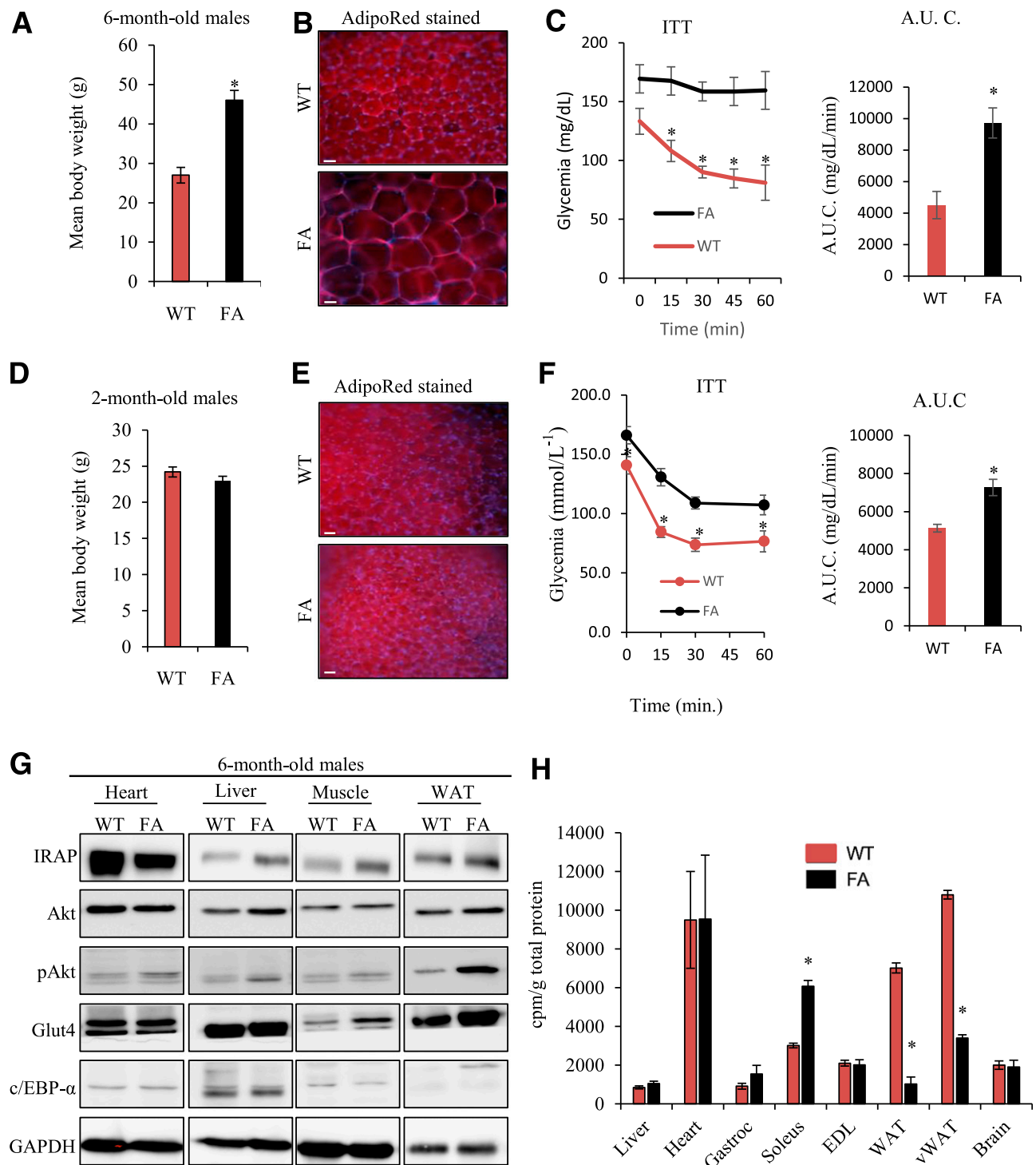
Figure 3—Metabolic characterization of FA mice. *A*: Mean body weight from 6-month-old male mice. *B*: Visceral AT from 6-month-old male mice stained with AdipoRed. *C*: ITT and corresponding histogram showing AUC $P < 0.001$ from 6-month-old male mice. *D*: Mean body weight from 2-month-old male mice. *E*: Visceral AT from 2-month-old male mice stained with AdipoRed. *F*: ITT and histogram showing AUC from 2-month-old male mice. *G*: Immunoblots of insulin signaling-related proteins in tissues from 6-month-old mice. *H*: Measurement of insulin-stimulated deoxyglucose uptake levels in 2-month-old mice ($n = 8$ mice per genotype). Scale bar, 25 μmol/L. WT, wild type.

resulting reactivation of *Alms1* expression specifically in adipocytes (Fig. 4*A*) was associated with a loss of the obesity phenotype for the *Alms^flin/flin^; Adipo-Cre^+/−^* compared with *Alms^flin/flin^* mice, which became obese in their

first 3 months (Fig. 4*B*), exhibiting adipocyte hypertrophy, similar to the human ALMS data (Fig. 4*C*). This obesity and adipocyte hypertrophy reverted when AT *Alms1* expression was restored in the *Alms^flin/flin^; Adipo-Cre^+/−^* mice (Fig. 4*C*).
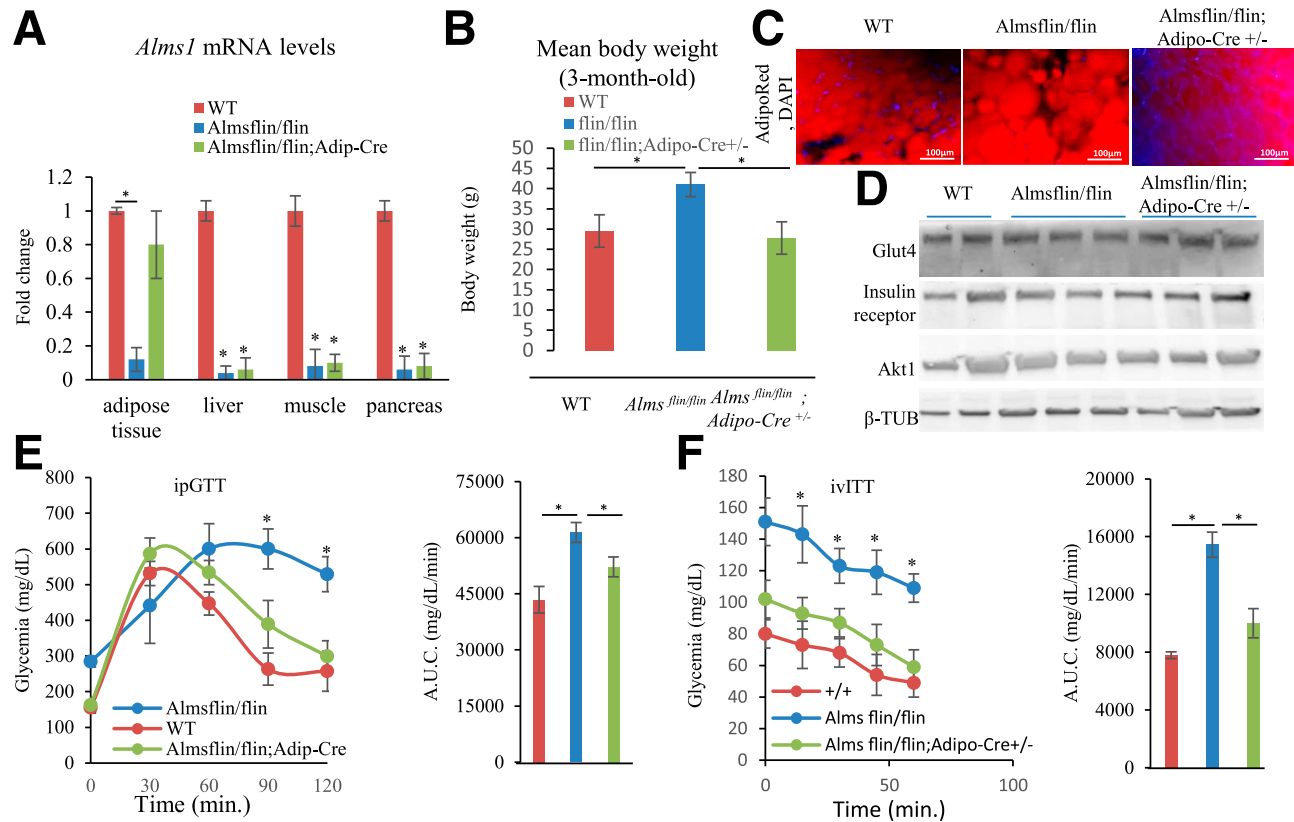
Figure 4—Metabolic characterization of $Alms^{flin/flin}$ and $Alms^{flin/flin}$; $Adipo\text{-}Cre^{+/-}$ mice. A: Fold change in Alms1 expression levels measured by real-time PCR in the indicated tissues for the given genotypes. Gapdh as reference gene. $n = 5$ per group with significance set at $*P < 0.01$. B: Mean body weight from 3-month-old male mice on chow diet. $n = 8$ per group with significance set at $*P < 0.05$. C: Visceral AT from 3-month-old male mice stained with AdipoRed. D: Immunodetection of GLUT4, insulin receptor, AKT serine/threonine kinase 1 (AKT1), and β-tubulin (β-tubulin) in 3-month-old visceral AT (25 μg total protein loaded per lane). E: Intraperitoneal GTT (ipGTT) and corresponding histogram showing AUC $P < 0.005$ from 3-month-old male mice. F: Intravenous ITT (ivITT) and corresponding histogram showing AUC $P < 0.001$ from 3-month-old male mice. β-TUB, β-tubulin; WT, wild type.

Immunodetection of AKT, GLUT4, and insulin receptor in the visceral AT extracts was similar for the three tested genotypes (Fig. 4D) with no significant differences upon ImageJ quantification (data not shown). At 3 months old, $Alms^{flin/flin}$ mice exhibited significant fasting hyperglycemia, glucose intolerance, and IR on both GTT (Fig. 4E) and ITT (Fig. 4F) compared with their wild-type littermates. By comparison, glucose tolerance and IR reverted to normal in $Alms^{flin/flin}$ mice when Alms1 expression was restored exclusively in the AT (Fig. 4E and F).

ALMS1 Plays a Role in Insulin-Stimulated Glucose Uptake in Human Adipocytes

Given the evidence of AT-driven IR both in ALMS participants and the three types of mouse models suggesting a key role for Alms1 in insulin-regulated glucose homeostasis, we knocked down ALMS1 in mature human adipocytes using a commercial ALMS shRNA lentivirus (Fig. 5A). We assessed the effect on glucose absorption using the fluorescent glucose analog, 2-NBDG. In the absence of insulin stimulation, 2-NBDG uptake was not seen in control or ALMS1-silenced adipocytes (Fig. 5B). Upon insulin stimulation, 2-NBDG uptake was significantly increased in control but

not in ALMS1-silenced adipocytes (Fig. 5C and D). This difference was not related to impaired AKT phosphorylation, a key mediator of insulin signaling in adipocytes; p-S473-AKT levels were readily detected after 30 min incubation with insulin in both control and ALMS1-silenced adipocytes (Fig. 5E). We also checked the possible impact of ALMS1 silencing on adipogenesis. Following ALMS1 knockdown in preadipocytes (Supplementary Fig. 4A), we measured the expression levels of classical adipogenic markers during differentiation. Although a significant decrease in the antiadipogenic factor PREF-1 was observed (Supplementary Fig. 4B), no significant difference in expression of proadipogenic transcription factors such as the cEBPs and PPARγ was detected (Supplementary Fig. 4C–G), indicating that ALMS1 is not required for adipogenic differentiation. In parallel, following specific ALMS1 lentiviral-mediated knockdown in mature human adipocyte, we measured the mitochondrial marker expression level of UCP-1 and found a significant reduction of UCP-1 expression levels in ALMS1-deprived mature adipocytes compared with controls (Supplementary Fig. 4H), denoting that ALMS1 inactivation also impacts mitochondrial function.
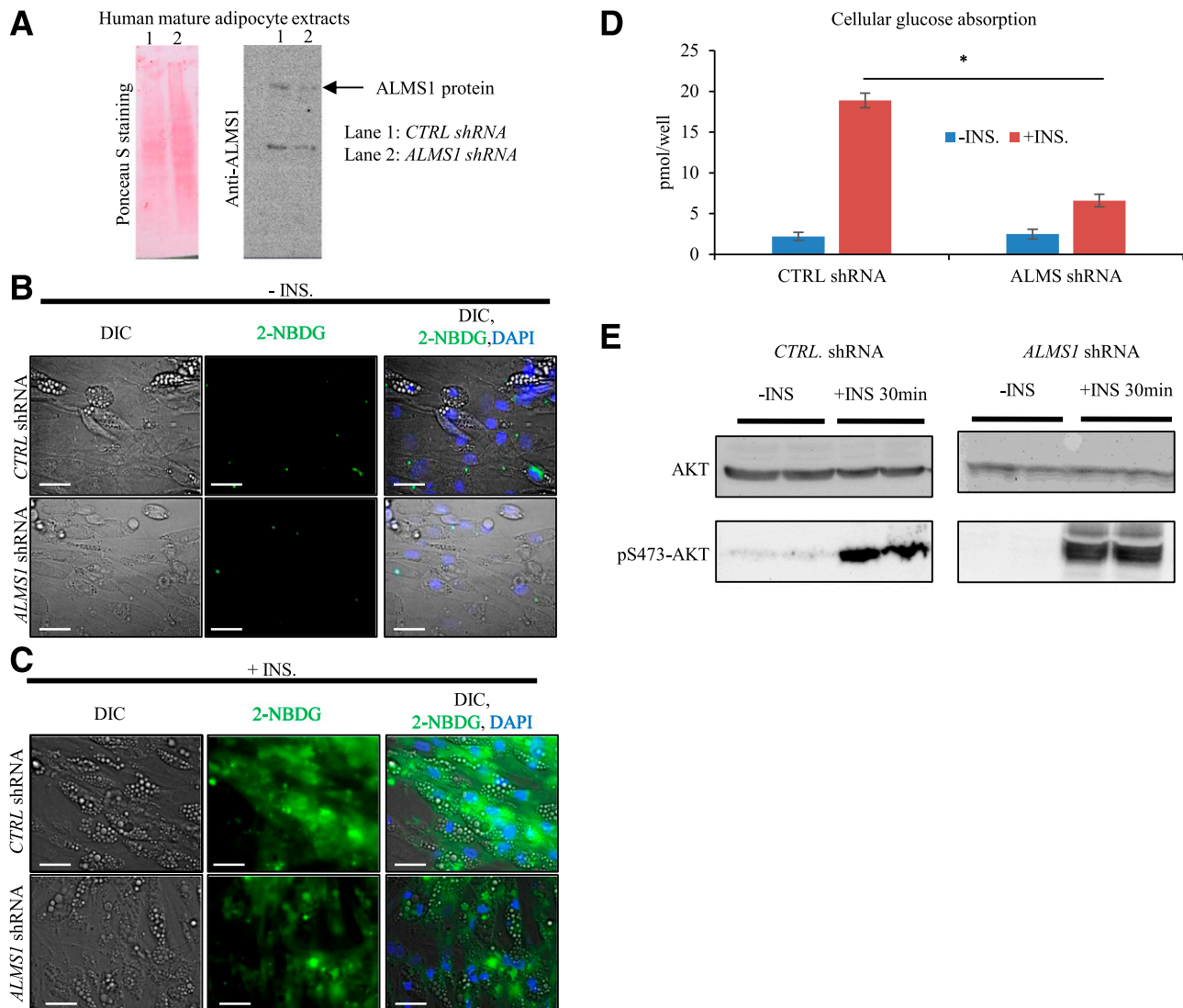
Figure 5—ALMS1 silencing impairs glucose absorption downstream of AKT phosphorylation step. *A*: Representative Ponceau S staining (left) and immunodetection of ALMS1 protein at 460 kDa (right) on cellular extracts from either control-shRNA-treated or ALMS1-shRNA-treated adipocytes. *B*: Photographs of 2-NBDG (green) in control or *ALMS1*-silenced mature adipocytes in absence of insulin. DIC, differential interference contrast pictures. *C*: Photographs of 2-NBDG uptake in presence of insulin. Scale bar, 20 μm. *D*: Quantification of cellular glucose absorption in treated human adipocytes ($n = 8$ wells per group). *E*: Immunodetection of AKT and p-S473-AKT on mature adipocyte cell lysates in presence and absence of insulin. *CTRL*, control; INS, insulin.

DISCUSSION

The data presented herein provide new insights into the relationship between obesity and IR. Firstly, our detailed phenotyping of a human ALMS monogenic obese cohort revealed a relative AT failure. Secondly, Alms1 gene inactivation in the mouse recapitulated the metabolic profile of human ALMS. Furthermore, complementing the human and mouse in vivo data, Alms1 inactivation in adipocyte was shown to specifically inhibit adipocyte glucose absorption. Third, reactivation of Alms1 gene only in the AT of Adipo-Cre$^{+/-}$ mice reversed obesity, systemic IR, and glucose intolerance. Taken together, these results indicate that in ALMS, AT dysfunction is a major determinant in driving whole-body systemic IR.

We observed a disproportionately severe degree of IR and its attendant complications in participants with ALMS compared with matched control subjects with common obesity. A recent study of 38 participants showed no difference in body fat distribution between ALMS participants and matched obese control subjects (6), providing evidence that the disproportionately high rate of IR and type 2 diabetes in ALMS is not due to differences in relative fat distribution or sarcopenia.

A growing body of evidence indicates that the primary defect leading to systemic IR occurs in AT. Maintenance of a high degree of flexibility in cell architecture and surrounding extracellular matrix network has been reported as a prerequisite for healthy AT (19). The dramatic increase

we have observed in adipocyte size in ALMS may reflect that ATs undergo rapid turnover and de novo formation. Approximately 10% of fat cells are renewed annually in adults, and it has been highlighted that adipocyte development and differentiations play a key role in the etiology of obesity and subsequent IR (20,21). Our findings of larger and heterogeneous adipocytes proportionate to the level of IR but discordant to the level of adiposity indicate the metabolic inflexibility of AT in the context of a chronic metabolic stressor (excess caloric intake) in our monogenic obese cohort. Similarly, adipocyte hypertrophy is a recognized feature of dysfunctional AT that is associated with increased cellular stress, hypoxia, and inflammation, and a threshold may be reached beyond which further hypertrophy impairs adipocyte metabolic flexibility (22,23). Furthermore, we found no evidence of excess pericellular or total fat fibrosis between the two obese cohorts. Existing evidence addressing the functional consequences of AT fibrosis are a matter of considerable debate as to whether fibrosis is an adaptive or maladaptive process of obesity (24). In line with our hypothesis of relative AT failure as a driver of IR, we have shown severe AT dysfunction without fibrosis in moderately obese patients with ALMS compared with control subjects. This is the first study showing relative AT failure in a human obesity. ALMS may represent an intermediary phenotype between lipodystrophy and extreme obesity, distinguished by a low threshold for expression of relative adipose failure, but without frank anatomical deficiency of AT.

Our two types of Alms1-deficient mouse models (naturally occurring and knockout) recapitulated the profound systemic IR we have observed in human ALMS subjects. This is consistent with a previously reported Alms1 knockout mouse model where they have observed high levels of obesity and IR (5). Furthermore, using Alms1 knockout primary human adipocytes and mouse models, we have shown the direct contribution of Alms1 protein in glucose homeostasis in AT and the subsequent consequence for other gluconeogenic organs in driving the whole-body systemic IR.

The precise role of Alms1 in adipocyte biology is not fully understood, and expression decreases at an early stage in adipocyte differentiation and is not altered by treatments known to effect differentiation (25). However, knockdown experiments have shown that reduced Alms1 expression decreases adipogenesis and lipid accumulation, although proximal insulin action is preserved (13). Alms1 knockout mice gain weight rapidly on a high-fat diet (6 weeks) with AT mass expansion. However, with increasing time on a high-fat diet (up to 24 weeks), AT mass fails to expand further, contrasting with observations in wild-type animals, and yet systemic IR has increased, indicating AT dysfunction (26). The amelioration of systemic IR by selective reactivation of Alms1 gene only in the AT in ($Alms^{flin/flin}$; $Adipo$-$Cre^{+/-}$) mice provides compelling evidence that AT dysfunction alone, in this monogenic

cohort, is the sole primary cause to induce systemic IR. Although AT is not quantitatively important as a site of postprandial glucose disposal compared with skeletal muscle, it does exert major remote effects on insulin sensitivity in muscle, liver, and other tissues (27,28).

It is now well established that AT is pivotal in regulating overall glucose homeostasis, but what remained to be demonstrated is how a tissue that absorbs a minimal 20% of overall circulating levels of glucose can trigger such profound deleterious metabolic impacts when it becomes dysfunctional. Impaired adipocyte glucose transport in AT-conditional GLUT4 knockout mice has been shown to be sufficient to drive whole-body extreme IR and type 2 diabetes (29,30). Glucose entry into AT activates carbohydrate-response element–binding protein (ChREBP), which has been directly linked to whole-body insulin sensitivity (31). Furthermore, healthy adipocytes release a lipokine, a lipid hormone linking AT to systemic insulin sensitivity (32). In addition, it has been established that two-thirds of all hepatic lipid content originate from AT, which indicates that any change will inevitably impact on the liver (33). The interesting observation that ALMS patients develop obesity despite impaired glucose absorption prompted us to hypothesize that the adipocyte switches cellular fuel from glucose to lipid utilization—an energy tropism switch that comes at a cost where the adipocyte starts secreting unhealthy signals and triggers a deleterious effect on a whole-body level. Similarly, any entity that restores physiological energy usage in the adipocyte will probably improve whole-body metabolic dysfunctions—a hypothesis that warrants further investigation.

In conclusion, we have shown for the first time that relative AT failure in obesity drives systemic IR. Our result showed the power of deep phenotyping of an ultra-rare monogenic disease to better understand common diseases of epidemic proportions and presented the first tractable genetically defined obese human model to study metabolic syndromes. Further studies are under way in exploring the mechanism by which ALMS1 protein alteration results in severe IR.

Author Contributions. T.G. and V.M. conceived and designed the study. S.B. recruited the study participants and performed HEC and fat biopsy. C.O., D.G., and N.M. performed in vitro and in vivo experiments. All authors analyzed the data. T.G., S.B., J.W.T., R.P.S., H.D., and N.P. helped in drafting the manuscript. All

authors reviewed the draft and approved the final version. T.G. and V.M. are the guarantors of this work and, as such, had full access to all the data in the study and take responsibility for the integrity of the data and the accuracy of the data analysis.

References

1. Marshall JD, Bronson RT, Collin GB, et al. New Alström syndrome phenotypes based on the evaluation of 182 cases. Arch Intern Med 2005;165:675–683

2. Girard D, Petrovsky N. Alström syndrome: insights into the pathogenesis of metabolic disorders. Nat Rev Endocrinol 2011;7:77–88

3. Paisey RB, Smith J, Carey C, et al. Duration of diabetes predicts aortic pulse wave velocity and vascular events in Alström syndrome. J Clin Endocrinol Metab 2015;100:E1116–E1124

4. Gathercole LL, Hazlehurst JM, Armstrong MJ, et al. Advanced non-alcoholic fatty liver disease and adipose tissue fibrosis in patients with Alström syndrome. Liver Int 2016;36:1704–1712

5. Collin GB, Marshall JD, Ikeda A, et al. Mutations in ALMS1 cause obesity, type 2 diabetes and neurosensory degeneration in Alström syndrome. Nat Genet 2002; 31:74–78

6. Han JC, Reyes-Capo DP, Liu CY, et al. Comprehensive endocrine-metabolic evaluation of patients with Alström syndrome compared with BMI-matched controls. J Clin Endocrinol Metab 2018;103:2707–2719

7. Paisey RB, Geberhiwot T, Waterson M, et al. Modification of severe insulin resistant diabetes in response to lifestyle changes in Alström syndrome. Eur J Med Genet 2014;57:71–75

8. Semple RK, Savage DB, Cochran EK, Gorden P, O'Rahilly S. Genetic syndromes of severe insulin resistance. Endocr Rev 2011;32:498–514

9. Virtue S, Vidal-Puig A. Adipose tissue expandability, lipotoxicity and the Metabolic Syndrome–an allostatic perspective. Biochim Biophys Acta 2010;1801: 338–349

10. Medina-Gomez G, Virtue S, Lelliott C, et al. The link between nutritional status and insulin sensitivity is dependent on the adipocyte-specific peroxisome proliferator-activated receptor-gamma2 isoform. Diabetes 2005;54:1706–1716

11. Carobbio S, Pellegrinelli V, Vidal-Puig A. Adipose tissue function and expandability as determinants of lipotoxicity and the metabolic syndrome. Adv Exp Med Biol 2017;960:161–196

12. Favaretto F, Milan G, Collin GB, et al. GLUT4 defects in adipose tissue are early signs of metabolic alterations in Alms1GT/GT, a mouse model for obesity and insulin resistance. PLoS One 2014;9:e109540

13. Huang-Doran I, Semple RK. Knockdown of the Alström syndrome-associated gene Alms1 in 3T3-L1 preadipocytes impairs adipogenesis but has no effect on cell-autonomous insulin action. Int J Obes 2010;34:1554–1558

14. Søndergaard E, Espinosa De Ycaza AE, Morgan-Bathke M, Jensen MD. How to measure adipose tissue insulin sensitivity. J Clin Endocrinol Metab 2017;102: 1193–1199

15. Ilias I, Apollonatou S, Nikitas N, et al. Microdialysis-assessed adipose tissue metabolism, circulating cytokines and outcome in critical illness. Metabolites 2018;8:62

16. Nikitas N, Kopterides P, Ilias I, et al. Elevated adipose tissue lactate to pyruvate (L/P) ratio predicts poor outcome in critically ill patients with septic shock: a microdialysis study. Minerva Anestesiol 2013;79:1229–1237

17. Stern JH, Rutkowski JM, Scherer PE. Adiponectin, leptin, and fatty acids in the maintenance of metabolic homeostasis through adipose tissue crosstalk. Cell Metab 2016;23:770–784

18. Arsov T, Silva DG, O'Bryan MK, et al. Fat aussie–a new Alström syndrome mouse showing a critical role for ALMS1 in obesity, diabetes, and spermatogenesis. Mol Endocrinol 2006;20:1610–1622

19. Sun K, Kusminski CM, Scherer PE. Adipose tissue remodeling and obesity. J Clin Invest 2011;121:2094–2101

20. Rosen ED, Spiegelman BM. What we talk about when we talk about fat. Cell 2014;156:20–44

21. Kahn CR, Wang G, Lee KY. Altered adipose tissue and adipocyte function in the pathogenesis of metabolic syndrome. J Clin Invest 2019;129:3990–4000

22. Rutkowski JM, Stern JH, Scherer PE. The cell biology of fat expansion. J Cell Biol 2015;208:501–512

23. Spalding KL, Arner E, Westermark PO, et al. Dynamics of fat cell turnover in humans. Nature 2008;453:783–787

24. Datta R, Podolsky MJ, Atabai K. Fat fibrosis: friend or foe? JCI Insight 2018;3: e122289

25. Romano S, Milan G, Veronese C, et al. Regulation of Alström syndrome gene expression during adipogenesis and its relationship with fat cell insulin sensitivity. Int J Mol Med 2008;21:731–736

26. Arsov T, Larter CZ, Nolan CJ, et al. Adaptive failure to high-fat diet characterizes steatohepatitis in Alms1 mutant mice. Biochem Biophys Res Commun 2006;342:1152–1159

27. Ying W, Wollam J, Ofrecio JM, et al. Adipose tissue B2 cells promote insulin resistance through leukotriene LTB4/LTB4R1 signaling. J Clin Invest 2017;127: 1019–1030

28. Xu H, Barnes GT, Yang Q, et al. Chronic inflammation in fat plays a crucial role in the development of obesity-related insulin resistance. J Clin Invest 2003;112: 1821–1830

29. Abel ED, Peroni O, Kim JK, et al. Adipose-selective targeting of the GLUT4 gene impairs insulin action in muscle and liver. Nature 2001;409:729–733

30. Minokoshi Y, Kahn CR, Kahn BB. Tissue-specific ablation of the GLUT4 glucose transporter or the insulin receptor challenges assumptions about insulin action and glucose homeostasis. J Biol Chem 2003;278:33609–33612

31. Herman MA, Peroni OD, Villoria J, et al. A novel ChREBP isoform in adipose tissue regulates systemic glucose metabolism. Nature 2012;484:333–338

32. Cao H, Gerhold K, Mayers JR, Wiest MM, Watkins SM, Hotamisligil GS. Identification of a lipokine, a lipid hormone linking adipose tissue to systemic metabolism. Cell 2008;134:933–944

33. Shulman GI. Ectopic fat in insulin resistance, dyslipidemia, and cardiometabolic disease. N Engl J Med 2014;371:2237–2238

34. Baig S, Veeranna V, Bolton S, et al. Treatment with PBI-4050 in patients with Alström syndrome: study protocol for a phase 2, single-centre, single-arm, open-label trial. BMC Endocr Disord 18;18:88

35. Finegood DT, Bergman RN, Vranic M. Estimation of endogenous glucose production during hyperinsulinemic-euglycemic glucose clamps. Comparison of unlabeled and labeled exogenous glucose infusates. Diabetes 1987;36: 914–924

36. Jentjens RL, Underwood K, Achten J, Currell K, Mann CH, Jeukendrup AE. Exogenous carbohydrate oxidation rates are elevated after combined ingestion of glucose and fructose during exercise in the heat. J Appl Physiol (1985) 2006;100: 807–816

37. Armstrong MJ, Hazlehurst JM, Hull D, et al. Abdominal subcutaneous adipose tissue insulin resistance and lipolysis in patients with non-alcoholic steatohepatitis. Diabetes Obes Metab 2014;16:651–660

38. Divoux A, Tordjman J, Lacasa D, et al. Fibrosis in human adipose tissue: composition, distribution, and link with lipid metabolism and fat mass loss. Diabetes 2010;59:2817–2825

39. Bel Lassen P, Charlotte F, Liu Y, et al. The FAT score, a fibrosis score of adipose tissue: predicting weight-loss outcome after gastric bypass. J Clin Endocrinol Metab 2017;102:2443–2453